

# Synchronous Differential Hot-charge Emission Spectroscopy: The Principle

Xuan Ji<sup>1,2,†,\*</sup>, Wen Chen<sup>1,2,†</sup>, Xi Yu<sup>1,2,\*</sup>

1. *State Key Laboratory of Advanced Materials for Intelligent Sensing, Key Laboratory of Organic Integrated Circuit, Ministry of Education & Tianjin Key Laboratory of Molecular Optoelectronic Sciences, Department of Chemistry, School of Science, Tianjin University, Tianjin 300072, China.*
2. *Collaborative Innovation Center of Chemical Science and Engineering (Tianjin), Tianjin 300072, China.*

† These authors contributed equally to this work.

\* Corresponding authors: Xuan Ji [jixuan\\_0808@tju.edu.cn](mailto:jixuan_0808@tju.edu.cn), Xi Yu [xi.yu@tju.edu.cn](mailto:xi.yu@tju.edu.cn).

## Abstract

Energy-level alignment (ELA) at buried interfaces between electrode and molecular materials sets charge injection barriers, carrier selectivity, and ultimately device efficiency, yet it is challenging to quantify under operating conditions. Hot-charge emission spectroscopy (HotES) probes ELA by injecting ballistic carriers across a tunneling oxide. Yet, the technique inherently convolutes the molecular response with a strong, energy-dependent tunneling background, complicating the isolation of the true ELA. We introduce synchronous differential HotES (sd-HotES), defined as the ratio of the differential conductance of the hot-charge and tunneling channels of the HotES. Physical modeling and numerical simulations validate that this ratio directly reconstructs the intrinsic molecular charge transmission, enabling the threshold-free and probe-bias-insensitive

extraction of ELA. By effectively eliminating the masking tunneling background, sd-HotES substantially boosts detection sensitivity; weak spectral features previously hidden in conventional HotES become clearly resolvable, as demonstrated in lock-in simulations including realistic noise. This study establishes the fundamental operating principles of sd-HotES and highlights it as a powerful, broadly applicable strategy for accessing buried interface properties for the study of molecular and hybrid devices.

## Introduction

Energy-level alignment (ELA) at buried molecule-metal interfaces is a primary determinant of charge-transport characteristics and overall device function in molecular and organic electronics<sup>1-4</sup>. By setting the relative positions of molecular frontier orbitals and electrode Fermi levels, ELA defines injection barriers for electrons and holes, governs carrier selectivity at contacts, and thus controls device functionality and efficiency<sup>5</sup>. Moreover, ELA undergoes evolving under the influence of interface dipoles<sup>6,7</sup>, image-charge screening by the metal substrate<sup>8,9</sup>, bias-induced molecular polarization<sup>10</sup>, and other non-equilibrium effects that emerge only under operating conditions. Consequently, accurate *in situ* quantification of ELA yet remains a significant challenge.

Established *ex situ* probes, including cyclic voltammetry<sup>11</sup> and ultraviolet photoelectron/inverse photoelectron spectroscopy<sup>12,13</sup> report redox potentials in solutions or band edges in films, referenced to different energy baselines and microenvironments<sup>14,15</sup>. As a result, they systematically misrepresent buried injection barriers in functioning devices<sup>16</sup>. *In-device* electrical analyses, such as transition-voltage spectroscopy (TVS)<sup>17,18</sup> and I-V characteristics analysis<sup>19,20</sup>, typically rely on charge transport mechanisms and strong assumptions about contact asymmetry<sup>21</sup>, voltage division<sup>22</sup>, and channel multiplicity<sup>23,24</sup>. While

advanced techniques like ultrafast laser-triggered tunneling can resolve molecular resonances, they are hindered by weak signals and prohibitive instrumental complexity<sup>25,26</sup>. These limitations motivate an *in-device*, bias-free technique that directly and quantitatively characterize the level alignment under device-operating conditions.

Hot-electron emission spectroscopy (HotES)<sup>27–30</sup>, along with ballistic electron emission spectroscopy (BEES)<sup>31–33</sup>, provides such a route. In this geometry, a tunnel junction injects ballistic carriers with tunable excess energy across a base electrode, while the collector circuit remains unbiased (Fig. 1). Ideally, the emitter bias directly maps ELA by driving current only at molecular resonances, a principle validated in Au/C<sub>60</sub> device where LUMO and LUMO+1 levels were successfully resolved<sup>27,34</sup>. However, the signal detected by the collector is dominated by the intense, energy-dependent transmission of the tunneling oxide (Fig. 1a, b). Consequently, the measurement inevitably convolutes the molecular response with this strong tunneling background, obscuring the intrinsic molecular signatures (Fig. 1c). Conventional extraction methods—whether based on threshold picking or linear extrapolation—yield values that deviate substantially from ELA benchmarks. Thus, prior analyses have relied on heuristic definitions of "turn-on" voltage, rendering the extracted ELA inherently subjective and unreliable.

In this work, we introduce synchronous differential HotES (sd-HotES) as a quantitative, threshold-independent probe of ELA at buried molecule-metal interfaces in device. In sd-HotES, the spectrum is defined as the ratio of the differential conductances of the tunneling and hot-charge collection channels. This derivative-ratio construction effectively divides out the strongly energy-dependent oxide transmission and removes the large base-tunneling background, thereby isolating and amplifying the much weaker molecular transmission signal.

We elucidate the physical principle using a theoretical model of oxide-mediated hot-charge injection convolved with the charge transport function of a molecular junction and established an exact correspondence under ideal conditions. We further derived the specific deviation between the sd-HotES features and the intrinsic transport function, which, under typical conditions, is typically within chemical accuracy ( $\sim 40$  meV) and follows a predictable trend that serves as a correction basis, defining the ultimate accuracy boundaries for experimental applications. Together, this framework transforms HotES into a practical metrology for threshold-free, probe-bias-insensitive extraction of ELA under device-operating conditions.

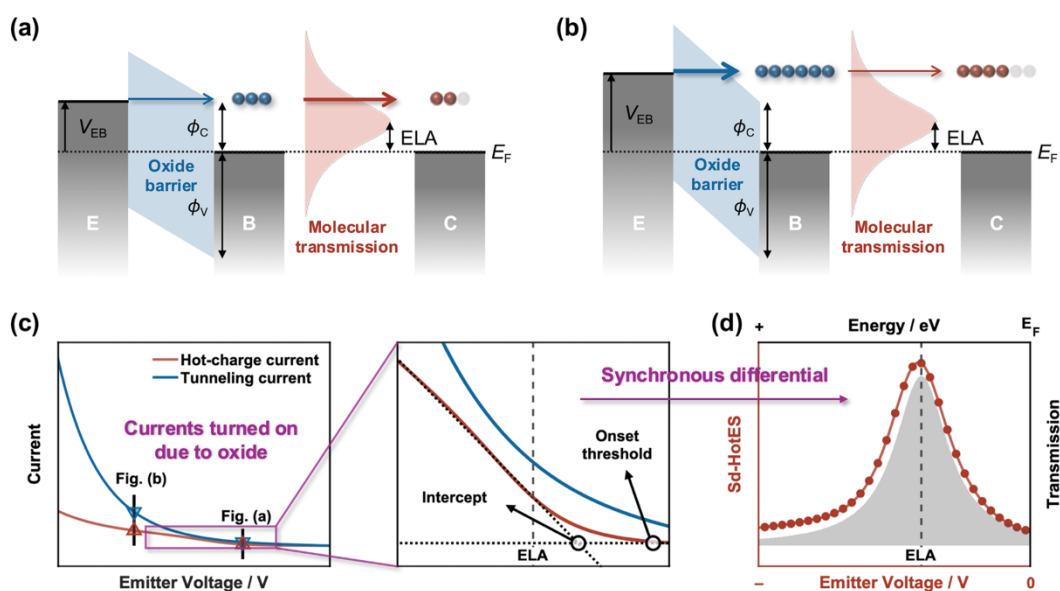


**Figure 1.** Schematic illustration of the principle of HotES and the synchronous differential HotES (sd-HotES) technique. (a, b) Energy diagrams under different emitter voltages. The oxide layer acts as an energy-selective filter for hot-carrier injection. (a) At lower emitter voltage, the large oxide barrier limits hot-charge injection despite favorable molecular conduction. (b) At higher emitter voltage, enhanced oxide tunneling provides more hot charges, even when the molecule is off resonance. (c) Hot-charge and tunneling currents. The vertical bars and marks correspond to transport behaviors depicted in energy diagrams (a,

b). (d) The sd-HotES spectrum (red) is compared with the molecular transmission (gray shadow), demonstrating successful isolation of molecular features, showing that sd-HotES spectrum can recover molecular transmission features.

## Theory and Model

### HotES and Synchronous Differential Formalism

The HotES measurement implements a three-terminal architecture, where an emitter–base tunneling junction, with an insulating dielectric layer, for example, aluminum oxide ( $\text{Al}_2\text{O}_3$ ) layer is in series with a base–collector molecular device between the base (B) and collector (C), as illustrated in Fig. 1a, b.

The experimental configuration employs the base electrode as the ground reference and hold the collector at the same potential ( $V_{\text{BC}} = 0$ ), ensuring zero bias across the channel while maintaining electrochemical equilibrium. Under these conditions, all three electrodes share the same Fermi level  $E_{\text{F}}$  at equilibrium. Applying a bias  $V_{\text{EB}}$  to the emitter shifts its chemical potential to  $\mu_{\text{E}} = E_{\text{F}} - eV_{\text{EB}}$  (taking the base Fermi level as energy zero,  $\mu_{\text{B}} = E_{\text{F}} = 0$ ). The emitter voltage thus acts as an energy selector that scans the energy-dependent transmission of the molecular layer without perturbing its electrochemical equilibrium.

Both emitter-base tunneling current and the base-collector hot-electron current can be expressed as energy integrals, in Landauer form<sup>29,35</sup>. The emitter-base current is:

$$I_{\text{EB}}(V_{\text{EB}}) = \frac{2e}{h} \int_{-\infty}^{+\infty} dE T_{\text{WKB}}(E; V_{\text{EB}}) [f_{\text{E}}(E; V_{\text{EB}}) - f_{\text{B}}(E)] \quad (1)$$

which provides a reference signal, where  $T_{\text{WKB}}(E; V_{\text{EB}})$  is the energy-dependent transmission probability through the  $\text{Al}_2\text{O}_3$  tunnel barrier under emitter voltage  $V_{\text{EB}}$ , and  $f_{\text{K}}(E) = [1 + \exp(E - \mu_{\text{K}}/k_{\text{B}}T)]^{-1}$  are Fermi-Dirac distribution functions

for electrode K.

Hot charges that have tunneled into the base can subsequently traverse the molecular layer to reach the collector. Since electrons must overcome both barriers through sequential, independent scattering processes, the overall transmission is the product  $T_{\text{WKB}}(E; V_{\text{EB}}) \cdot T_{\text{mol}}(E)$ . With  $V_{\text{BC}} = 0$  ensures  $\mu_{\text{C}} = \mu_{\text{B}}$ , the driving force is the same emitter-base chemical potential difference, and the hot-electron current is therefore expressed as:

$$I_{\text{BC}}(V_{\text{EB}}) = \frac{2e}{h} \int_{-\infty}^{+\infty} T_{\text{WKB}}(E; V_{\text{EB}}) \cdot T_{\text{mol}} \cdot [f_{\text{E}}(E; V_{\text{EB}}) - f_{\text{B}}(E)] dE \quad (2)$$

where  $T_{\text{mol}}(E)$  represents the molecular layer transmission at energy  $E$ . It is therefore not surprising that the hot-charge current  $I_{\text{BC}}(V_{\text{EB}})$ , which is the primary observable in conventional HotES, exhibits a line shape dominated by the oxide response, making threshold picking unreliable and molecular features difficult to discern.

To isolate the molecular transmission characteristics, a synchronous differential measurement strategy can be applied. In a single continuous sweep of  $V_{\text{EB}}$ , one can record simultaneously the differential conductance of the emitter-base junction  $G_{\text{Tunn}}(V_{\text{EB}}) = dI_{\text{EB}}/dV_{\text{EB}}$ , and that of the hot current  $G_{\text{Hot}}(V_{\text{EB}}) = dI_{\text{BC}}/dV_{\text{EB}}$ . Differentiating Eq. 1 and 2 under the integral sign and applying the chain rule yields:

$$G_{\text{Tunn}}(V_{\text{EB}}) = \frac{2e}{h} \int dE K(E; V_{\text{EB}}) \quad (3a)$$

$$G_{\text{Hot}}(V_{\text{EB}}) = \frac{2e}{h} \int dE T_{\text{mol}}(E) K(E; V_{\text{EB}}) \quad (3b)$$

where all bias dependence is encapsulated in an energy kernel function  $K(E; V_{\text{EB}})$  that represents the spectral weighting of electrons contributing to the differential

conductance at a given emitter bias, and is explicitly:

$$K(E; V_{\text{EB}}) = \frac{\partial T_{\text{WKB}}(E; V_{\text{EB}})}{\partial V_{\text{EB}}} [f_{\text{E}}(E; V_{\text{EB}}) - f_{\text{B}}(E)] + T_{\text{WKB}}(E; V_{\text{EB}}) \left( e \frac{\partial f_{\text{E}}}{\partial E} \right) \quad (4)$$

which contains two physically distinct contributions: the first term captures bias-induced changes in the oxide transmission probability, while the second term arises from the shifting Fermi distribution of the emitter with applied bias.

The ratio of the differential conductances defines the sd-HotES spectrum as:

$$R(V_{\text{EB}}) \equiv \frac{G_{\text{Hot}}(V_{\text{EB}})}{G_{\text{Tunn}}(V_{\text{EB}})} = \frac{\int dE T_{\text{mol}}(E) K(E; V_{\text{EB}})}{\int dE K(E; V_{\text{EB}})} \quad (5)$$

which, in essence, is a kernel-weighted average of the molecular transmission function. The kernel  $K(E; V_{\text{EB}})$  acts as an energy window function that localizes contributions near the emitter chemical potential  $\mu_{\text{E}} = E_{\text{F}} - eV_{\text{EB}}$ . Eq. 5 is the exact theoretical description of the sd-HotES, accounting for bias-induced changes in the oxide barrier shape and the finite-temperature broadening of the Fermi distribution.

In the idealized limit where the oxide barrier experiences minimal bias-induced deformation ( $\partial T_{\text{WKB}}/\partial V_{\text{EB}} \approx 0$ ) and low temperatures sharpen the Fermi distribution into a delta function  $\partial f/\partial E \rightarrow \delta(E - \mu_{\text{E}})$ , the energy kernel simplifies to:

$$K(E; V_{\text{EB}}) \propto T_{\text{WKB}} \delta(E - E_{\text{F}} + eV_{\text{EB}}) \quad (6)$$

Therefore, the conductance ratio  $R$  directly maps molecular transmission:

$$R(V_{\text{EB}}) = T_{\text{mol}}(E = E_{\text{F}} - eV_{\text{EB}}) \quad (7)$$

This relation captures the core idea of sd-HotES: the derivative ratio measurement factors out the strongly energy-dependent oxide transmission and yields a one-to-one mapping between the sd-HotES spectrum and the intrinsic molecular

transmission. It also establishes a simple "voltage-energy" correspondence that a negative emitter voltage  $V_{\text{EB}}$  probes molecular states at positive energies  $U \equiv E_{\text{F}} - eV_{\text{EB}} > 0$  above the Fermi level, and vice versa. In this way, the synchronous differential formalism elegantly uses the oxide tunneling barrier both as energy filter and built-in reference. By simultaneously monitoring the total injected current and the transmitted hot-charge current, and then taking their differential conductance ratio, sd-HotES effectively divides out the background contributions of the injector.

## **Transport Modeling of HotES Components**

### **The tunneling junction**

Electron tunneling across the  $\text{Al}_2\text{O}_3$  emitter-base junction is modeled within a classical one-dimensional Wentzel-Kramers-Brillouin (WKB) approximation as shown in Eq. 1<sup>36</sup>. Under an applied emitter voltage  $V_{\text{EB}}$ , the large-gap  $\text{Al}_2\text{O}_3$  dielectric<sup>37</sup>, with a conduction band barrier  $\phi_{\text{C}}$  and valence band barrier  $\phi_{\text{V}}$ , develops a tilted band profile, producing a trapezoidal potential barrier whose shape and height depend on bias (see Fig. 1a, b). This model captures the evolution of the oxide transmission  $T_{\text{WKB}}(E; V_{\text{EB}})$  from wide nearly rectangular barrier, to Fowler–Nordheim tunneling with a triangular barrier at higher bias. Detailed equations and simulation results are provided in Section S1 of the Supporting Information. In the context of sd-HotES, this tunneling module sets the energy-dependent filter that defines the kernel  $K(E; V_{\text{EB}})$  entering the synchronous differential formalism.

### **Charge transmission function of the molecular layer**

To further illustrate the sd-HotES principle and validate its efficacy, we model the actual charge transmission function of the molecular layer,  $T_{\text{mol}}(E)$ , using two canonical transport mechanisms widely established in molecular electronics. It is



important to note that these specific models serve primarily to parameterize numerical simulations of the sd-HotES spectra, allowing us to demonstrate how the technique enhances sensitivity and to quantify the correspondence between the measured signal and the intrinsic molecular transmission. As derived in the theoretical framework above, the sd-HotES signal is effectively a kernel-weighted average of the actual molecular transmission; therefore, while we select specific models here for demonstration, the validity of the sd-HotES methodology is general and independent of the specific form of  $T_{\text{mol}}(E)$ .

We examine single-state transport via two limiting mechanisms<sup>19,38,39</sup>: coherent tunneling through discrete molecular orbitals and incoherent hopping via sequential electron transfer.

For coherent transport, we employ the Landauer-Büttiker formalism<sup>40</sup>, where the transmission function through a single molecular orbital is described by a Lorentzian line shape arising from molecule-electrode coupling:

$$T_{\text{mol}}(E) = \frac{\Gamma^2}{(E - \varepsilon)^2 + (\Gamma/2)^2} \quad (8)$$

where  $\varepsilon$  represents the energy alignment of the molecular orbital (e.g., LUMO) relative to the Fermi level, and  $\Gamma$  denotes the broadening of the energy level due to hybridization with the electrodes. This model captures the resonance features typical of rigid molecular junctions at low temperatures.

For incoherent hopping, transport is governed by thermally activated electron transfer coupled to nuclear reorganization<sup>41</sup>. We apply the semi-classical Marcus theory, where the transmission probability is approximated by a Gaussian function, dominated by the rate of electron injection from hot-charge states into the molecule or extraction from the molecule to hot-charge states<sup>42</sup>:

$$T_{\text{mol}}(E) = k_0 \frac{1}{\sqrt{4\pi\lambda k_B T}} \exp \left[ -\frac{(\pm(\Delta E - E) + \lambda)^2}{4\lambda k_B T} \right] \quad (9)$$

Here,  $\lambda$  is the reorganization energy,  $T$  is the temperature,  $k_B$  is the Boltzmann constant,  $k_0$  is the quantum transition rate prefactor quantitatively related to the interfacial coupling parameter in the Landauer picture through  $k_0 = 2\Gamma/\hbar$ , and  $\Delta E$  is the energy difference between the reduced and oxidized state of the molecular system. The  $\pm$  sign accounts for hot electron (+, LUMO-mediated transport) and hole (−, HOMO-mediated transport) injection processes. This model describes broadened transport features significantly influenced by the vibrational environment and temperature.

By substituting these explicit forms of  $T_{\text{mol}}(E)$  into the synchronous differential formalism (Eq. 5) and integrating with the tunneling kernel derived from the oxide model, we can numerically simulate the resulting sd-HotES spectra. This approach allows us to rigorously evaluate the deviation between the extracted sd-HotES features and the intrinsic transport function, thereby establishing the accuracy limits and correction factors required for experimental analysis.

### **Inelastic scattering in base electrode**

Hot charges injected into the metal base undergo inelastic energy losses before they can cross into the subsequent molecular layer. The base thus acts as an energy redistribution medium, where non-equilibrium charges lose energy and relax towards the Fermi level through electron–electron and electron–phonon scattering over characteristic inelastic mean free paths (IMFP)<sup>29,43,44</sup>. The strong energy dependence of IMFP fundamentally determines what fraction remains sufficiently energetic to probe molecular states.

We describe this process using an energy-redistribution kernel  $s(E, E')$ <sup>29</sup>, which gives the probability for a carrier injected at energy  $E$  to arrive at energy  $E'$  while

remaining non-thermal population. The kernel accounts for both stepwise energy loss via inelastic scattering (characterized by energy-dependent IMFP) and catastrophic thermalization events. Detailed equations are provided in Section S2 of the Supporting Information. Incorporating this base scattering, the hot current generalizes to a double integral:

$$I_{\text{BC}} = \frac{2e}{h} \int dE T_{\text{WKB}}(E; V_{\text{EB}}) [f_{\text{E}}(E; V_{\text{EB}}) - f_{\text{B}}(E)] \int dE' s(E, E') T_{\text{mol}}(E') \quad (10)$$

This convolution of oxide filtering, base scattering, and molecular transmission shows how inelastic processes broaden the sharp energy selection imposed by the tunnel barrier, thereby setting the intrinsic energy resolution limit of sd-HotES.

## Results and discussion

We present a step-by-step validation of the sd-HotES framework, advancing from fundamental theoretical verification to realistic performance modeling. Our examination starts with the exact mapping of molecular transmission under ideal conditions, verifying the theoretical core of the method. We then introduce physical non-idealities, specifically scattering and barrier deformations, to demonstrate how sd-HotES effectively suppresses background signals where conventional methods fail. This is followed by a quantitative assessment of precision limits governed by oxide features. Finally, the study culminates in realistic lock-in simulations, confirming the method's practicality even in the presence of thermal noise.

### Analysis under ideal conditions

Fig. 2 presents comparisons across three levels of kernel approximation derived before for both tunneling and hopping transport at energies spanning HOMO and LUMO states, listed from top to bottom panels with transmission functions shown



4), yields well-defined peaks and whose positions correspond to the molecular orbital energies, though broader and with different intensities than ideal transmission. This validates that our kernel formalism captures the underlying physics of synchronous detection and provides direct experimental access to molecular electronic structure. The frozen barrier approximation (middle panel) treats oxide barrier transmission as bias-independent ( $\partial T_{\text{WKB}}/\partial V_{\text{EB}} = 0$ ), reducing the kernel to its second term with  $T_{\text{WKB}}(E; V_{\text{EB}} = 0)$ . This retains the energy selectivity of the oxide barrier while taking a weighted average of  $T_{\text{mol}}$  through a fixed  $T_{\text{WKB}}$  profile. The spectrum therefore dramatically converges toward the transmission function. Finally, the thermal-only kernel (bottom panel) further assumes  $T_{\text{WKB}}$  as a constant scale factor, leaving only the finite-temperature Fermi window to weight. Sd-HotES now nearly perfectly matches the molecular transmission, with correspondence that becomes exact in the low-temperature limit. This progressive convergence elegantly demonstrates that successive kernel simplifications remove extrinsic broadening, establishing the one-to-one connection. The primary remaining deviation source is bias-induced oxide barrier distortion, which redistributes the charge flux energy dependence away from ideal transmission profiles.

In addition, sd-HotES also offers richer physical insights in the hopping regime. Effective transmission and sd-HotES spectra exhibit peaks shifted from the defined energy difference (the charge-transfer driving force) by the reorganization energy, corresponding to  $\Delta E + \lambda$  for hot electron (negative emitter voltage) and  $\Delta E - \lambda$  for the hot hole (positive emitter voltage), in other words, vertical electron affinity or ionization potential, respectively. This indicates that single charge transfer is governed by IP and EA rather than bare energy differences, consistent with Marcus–Gerischer theory.<sup>45,46</sup> This connection between charge-transfer energetics and molecular orbital structure<sup>47,48</sup>, while noteworthy, lies beyond the primary

scope of this study and will be explored in detail elsewhere.

## Analysis under scattering conditions

Having established the formal principle of sd-HotES, we now demonstrate its performance under more realistic conditions where inelastic scattering in the base electrode redistributes hot-carrier energy and population, severely degrading the bias-orbital correspondence that underpins conventional threshold-based analysis on hot-charge currents.

Fig. 3a-d presents hot-charge currents for both tunneling and hopping transport. Traces are normalized to their respective maxima, with emitter-base tunneling current overlaid on a dual y-axis as a reference for shape comparison. We examine LUMO- and HOMO-dominated transport across several parameter combinations: varying molecular energy level alignment and coupling strength for tunneling, and adjusting charge-transfer energy differences, reorganization energies, and interfacial coupling strengths for hopping.

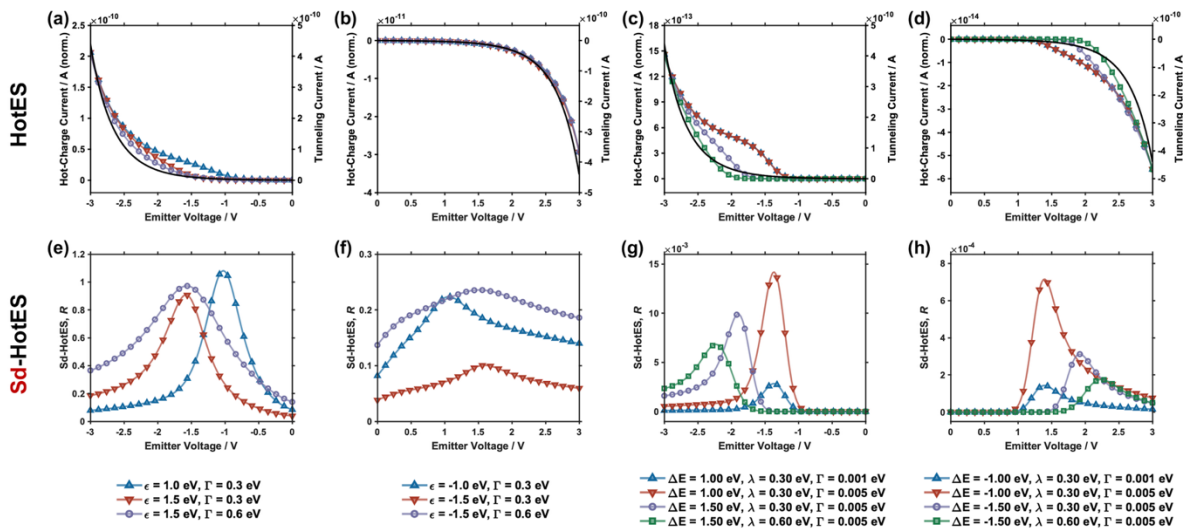


**Figure 3.** Hot-charge currents (a-d) and sd-HotES spectra (e-h) under base scattering conditions with varied parameter combinations for LUMO and HOMO conducting channels in tunneling (left panels) and hopping (right panels) transport. Hot-charge currents (colored

lines with scatters, left y-axis) are normalized to their respective maxima for clarity. Emitter–base tunneling current and its derivative (gray lines, right y-axis) serve as references. For tunneling transport, varied parameters include molecular energy level alignment and molecule–electrode coupling strength. For hopping transport, varied parameters include charge-transfer energy difference, reorganization energy, and interfacial coupling strength.

For LUMO-dominated tunneling transport (Fig. 3a), only a shallow current plateau appears around the resonance bias when the molecular levels lie near the Fermi energy with weak coupling. This feature rapidly washes out as levels move away from  $E_F$  or the coupling increases, rendering onsets happen together with Fowler–Nordheim transport of the oxide junction and molecular signatures nearly indistinguishable from the oxide background. For HOMO-dominated tunneling (Fig. 3b), hot-charge and tunneling currents are almost identical, consistent with a larger valence-band barrier in the base oxide that suppresses hot-carrier collection at positive bias. The hopping transport regime (Fig. 3c, d) exhibits analogous behavior. When driving forces are small and reorganization energies low, modest inflections appear around molecular charging thresholds (Fig. 3c), but higher bias invokes Fowler–Nordheim tunneling that obscures these signatures. HOMO-like hopping (Fig. 3d) exhibits even weaker signatures. Across both mechanisms, inelastic scattering smears molecular fingerprints into a broad background that closely tracks the smooth oxide tunneling profile, making genuine molecular features nearly impossible to distinguish from oxide artifacts using current measurements alone.

By contrast, the sd-HotES approach (Fig. 3e-h) resolves this issue by removing oxide background contributions. Spectra demonstrate pronounced peaks at molecular resonance voltages, with molecular signatures emerge distinctly across all parameter sets, where LUMO scenarios exhibit sharper, more prominent peak profiles than HOMO cases due to asymmetric energy barrier of the oxide layer.

Besides that, spectrum characteristics encode the underlying transport physics. In the tunneling scenario, the peak width correlates with molecule–electrode coupling strength, whereas for hopping, it corresponds to the reorganization energy associated with charge-transfer events. Quantum transition rates in hopping mainly modulate peak intensity rather than line shape. Peak position tracks molecular level alignment, orbitals closer to  $E_F$  produce larger peaks at lower bias, while more distant levels yield broader, weaker peaks at higher bias. Notably, even when energy levels lie far from  $E_F$  or broadening is substantial, i.e. conditions under which molecular transmission signatures are essentially invisible in raw hot-charge current traces, sd-HotES still reveals discernible peaks.

### **Systematic Accuracy and Detection Precision**

Establishing the practical utility of sd-HotES requires careful examination of its quantitative reliability and systematic accuracy. Even under ideal conditions, our earlier analysis in Fig. 2 revealed slight deviations in the sd-HotES peak shape relative to transmission function of the molecular layer. This residual discrepancy arises directly from the synchronous differential formalism defined in Eq. 5. The measured signal is not a direct readout of  $T_{\text{mol}}(E)$ , but rather its weighted average with the energy kernel  $K(E; V_{\text{EB}})$ . As detailed in the theoretical derivation, this kernel incorporates not only the thermal Fermi window but also a term governing the bias-induced deformation of the oxide barrier (Eq. 4). Because the oxide tunneling probability  $T_{\text{WKB}}(E; V_{\text{EB}})$  is inherently energy-dependent and sensitive to emitter bias, it introduces an asymmetric weighting to the integration. While the sd-HotES technique effectively divides out the bulk tunneling background, this varying spectral weight prevents the total elimination of barrier-induced distortions. Consequently, quantifying this systematic error, and understanding its dependence on device configuration and energy level position, is crucial for defining the precision limits and ensuring accurate interpretation of experimental



spectra.

To this, we scan the conduction band barrier  $\phi_C$  and valence band barrier  $\phi_V$  while maintaining the oxide bandgap within 7-9 eV (typical for  $\text{Al}_2\text{O}_3$ ), monitoring how the ELA extracted from the sd-HotES peak voltage  $V_{pk}$  derivates relative to the molecular transmission resonances. The corresponding TVS summit voltage, an indicator of nonlinear current characteristics, is simultaneously determined for each configuration.

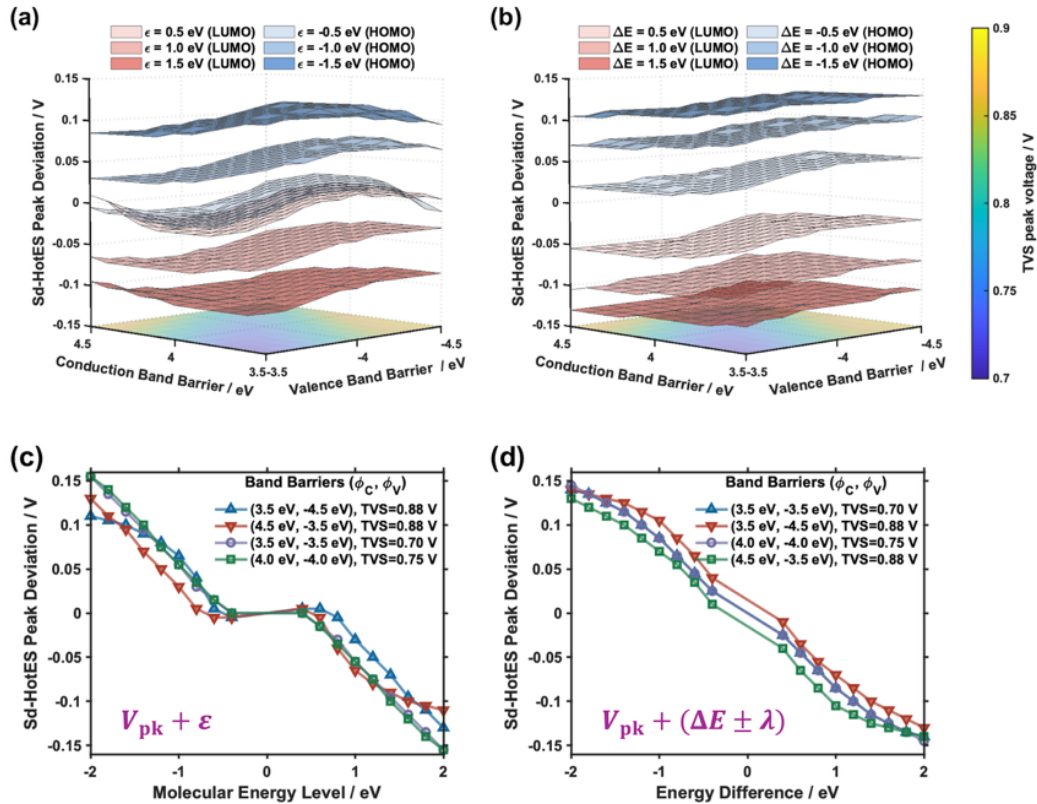


**Figure 4.** Numerical accuracy of sd-HotES extraction under base scattering conditions. 3D plots of deviation between sd-HotES peak positions and preset ELA (defined as  $V_{pk} + \epsilon$  for tunneling,  $V_{pk} + (\Delta E \pm \lambda)$  for hopping) as a function of oxide's band barrier heights for (a) tunneling (molecular energy levels) and (b) hopping (energy differences). Color bar indicates the TVS peak voltage at each band barrier combination. Peak deviation versus (c) molecular energy level for tunneling and (d) energy difference for hopping at fixed oxide barrier configurations. Other parameters are fixed at: interfacial coupling strength of 0.3 eV for

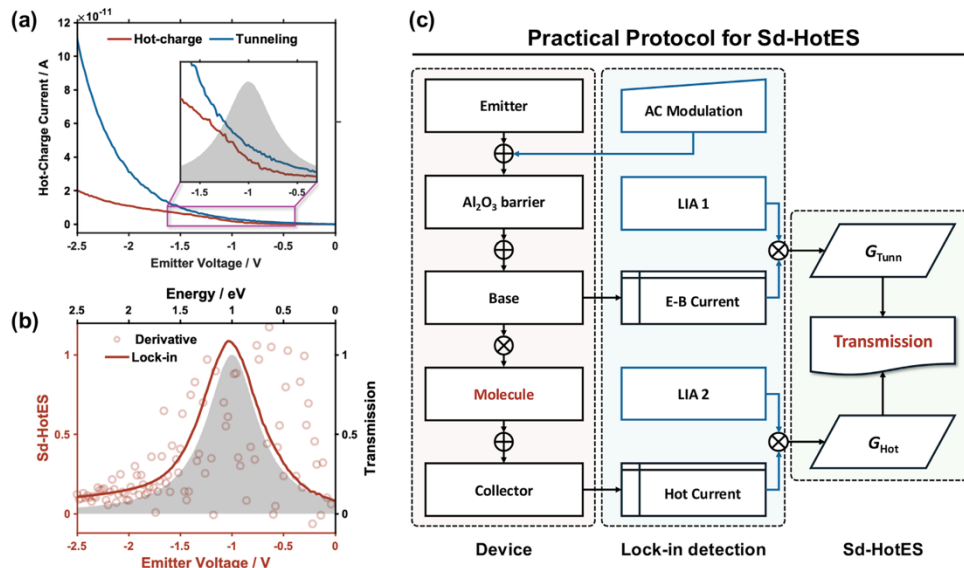
tunneling; reorganization energy of 0.3 eV and interfacial coupling of 0.005 eV for hopping. The 3D surfaces in Fig. 4a, b reveal the sensitivity of sd-HotES detection to oxide barrier configuration. For the shallow ELA near  $E_F$ , the surfaces exhibit strong fluctuations with error maintained within chemical accuracy, i.e.,  $\sim 40$  meV. In contrast, for deep-lying levels farther from  $E_F$ , the surfaces flatten, and measurement accuracy becomes less sensitive to specific barrier configurations. HOMO and LUMO levels show opposite deviation directions, each with optimal detection regimes. LUMO detection achieves minimal deviations when  $\phi_C$  is small and  $\phi_V$  is large, as hot electrons traverse the conduction band with higher flux and reduced energy redistribution. Conversely, HOMO detection favors large  $\phi_C$  and small  $\phi_V$ , enabling efficient hot-hole injection through the valence band with earlier resonance alignment.

Fig. 4c, d present cross-sectional analyses at fixed oxide barrier configurations, quantitatively demonstrating that sd-HotES detection accuracy decreases as ELA moves away from  $E_F$ . This trend stems primarily from enhanced inelastic scattering in the base, which strongly broadens and redistributes the energy-resolved hot charge population. For frontier orbitals (HOMO and LUMO) located within 1 eV of  $E_F$ , deviations remain minimal at about 0.05 eV across most configurations, demonstrating excellent precision for the device-relevant electronic states that govern charge injection efficiency and transport properties. Despite reaching deviations of 0.15 eV for ELA at 2 eV from  $E_F$  (HOMO1/LUMO+1 or beyond) sd-HotES provides a practical pathway for in-device characterization of multi-level electronic structure through bias-free, threshold-insensitive detection—capabilities challenging to existing methods, and Fig. 4c and d can be used as a correction map for practical sd-HotES measurement.

## Noise Resilience and Lock-in Simulation

Real-world laboratory measurements inevitably contend with noise sources that can obscure weak spectral features, particularly in high-impedance hot-carrier circuits. To evaluate the robustness of sd-HotES against these constraints, we explicitly incorporated Johnson–Nyquist noise into our transport models, simulating the dominant thermal fluctuations that scale with conductance and bandwidth. As illustrated in Fig. 5a for a representative tunneling case, the raw noise buries the subtle onsets and plateaus of the hot-charge current, rendering conventional threshold extraction and direct numerical differentiation of the DC current impossible.

To overcome this signal-to-noise limitation, we numerically simulated a synchronous lock-in amplification (LIA) protocol applied directly to the noisy data. Rather than simple differentiation, we mathematically replicated the full LIA signal chain: a small sinusoidal AC modulation ( $V_{AC} \sin \omega t$ ) was superimposed onto the DC emitter bias in the model, and the resulting current response was demodulated and low-pass filtered to extract the differential conductance. This process is schematized in Fig. 5c. The result of this simulation (Fig. 5b, solid line) demonstrates that the LIA processing effectively rejects the broadband noise floor. The sd-HotES peak is recovered with high fidelity, displaying position and width consistent with the noise-free idealization. This numerical validation confirms that synchronous lock-in detection is not merely an enhancement, but a critical and effective experimental protocol for implementing sd-HotES in practical laboratory settings.



**Figure 5.** (a) Hot-charge and tunneling currents under base-scattering conditions with Johnson-Nyquist thermal noise for a LUMO-conducting tunneling transport case. Parameters: molecular energy level at 1.0 eV and interfacial coupling strength of 0.3 eV, oxide barrier of 3.5 eV for conduction band and -4.5 eV for valence band. (b) Sd-HotES spectra obtained via direct numerical differentiation (open circles) and lock-in modulation (solid trace), compared with the ideal molecular transmission function (shaded profile). (c) Schematic workflow of lock-in modulation protocol for sd-HotES.

## Conclusion

This study establishes synchronous differential HotES (sd-HotES) as a quantitative metrological framework for probing the energetics of buried interfaces, advancing the technique beyond its traditional reliance on qualitative threshold determination. The central innovation lies in the synchronous differential ratio formalism, which utilizes the base tunneling response to suppress the strong, non-linear background of the oxide injector. By effectively "normalizing" the hot-carrier signal against this dynamic reference, sd-HotES reconstructs the characteristic spectral features of the interface, effectively overcoming the subjectivity inherent in conventional turn-on voltage analysis. This approach successfully resolves the

challenge of isolating weak interfacial signatures from high-background device currents, providing a direct and robust window into energy-level alignment under operating conditions.

Beyond theoretical validation, we have demonstrated the practical utility of sd-HotES as a rigorous experimental protocol. Our error analysis defines the systematic accuracy limits, confirming that the technique can achieve sufficient precision to resolve fine electronic features ( $< 40$  meV) relevant to device function. Furthermore, the implementation of synchronous lock-in detection ensures that this sensitivity is maintained even in the presence of thermal noise, offering a clear roadmap for standard laboratory deployment.

Looking forward, further research must focus on the rigorous experimental validation of this framework, particularly in complex systems where the intrinsic molecular transmission is unknown. A critical aspect of practical implementation remains the influence of the oxide layer. While sd-HotES relaxes the stringent requirement for high-barrier, highly linear tunneling oxides mandated by traditional HotES, the oxide's spectral features are not entirely eliminated from the measurement. Consequently, careful control of oxide quality and preparation conditions is imperative; comparative studies of molecular variations should employ identical oxide baselines to minimize background artifacts. For absolute quantification, the systematic deviation curves derived in this work serve as a necessary correction tool to mitigate residual barrier effects. Ultimately, while obtaining the exact transmission function of the oxide layer remains a challenge, future advances in characterizing  $T_{\text{WKB}}(E; V_{\text{EB}})$  could enable the complete mathematical deconvolution of the background, paving the way for absolute, artifact-free spectroscopy of buried interfaces.

## Literature

- (1) Ishii, H.; Sugiyama, K.; Ito, E.; Seki, K. Energy Level Alignment and Interfacial Electronic Structures at Organic/Metal and Organic/Organic Interfaces. *Adv. Mater.* **1999**, *11* (8), 605–625.
- (2) Braun, S.; Salaneck, W. R.; Fahlman, M. Energy-Level Alignment at Organic/Metal and Organic/Organic Interfaces. *Adv. Mater.* **2009**, *21* (14–15), 1450–1472. <https://doi.org/10.1002/adma.200802893>.
- (3) Xin, N.; Guan, J.; Zhou, C.; Chen, X.; Gu, C.; Li, Y.; Ratner, M. A.; Nitzan, A.; Stoddart, J. F.; Guo, X. Concepts in the Design and Engineering of Single-Molecule Electronic Devices. *Nat. Rev. Phys.* **2019**, *1* (3), 211–230. <https://doi.org/10.1038/s42254-019-0022-x>.
- (4) Fahlman, M.; Fabiano, S.; Gueskine, V.; Simon, D.; Berggren, M.; Crispin, X. Interfaces in Organic Electronics. *Nat. Rev. Mater.* **2019**, *4* (10), 627–650. <https://doi.org/10.1038/s41578-019-0127-y>.
- (5) Nitzan, A.; Ratner, M. A. Electron Transport in Molecular Wire Junctions. *Science* **2003**, *300* (5624), 1384–1389. <https://doi.org/10.1126/science.1081572>.
- (6) Xue, Y.; Datta, S.; Ratner, M. A. Charge Transfer and “Band Lineup” in Molecular Electronic Devices: A Chemical and Numerical Interpretation. *J. Chem. Phys.* **2001**, *115* (9), 4292–4299. <https://doi.org/10.1063/1.1391253>.
- (7) Heimel, G.; Romaner, L.; Zojer, E.; Bredas, J. L. The Interface Energetics of Self-Assembled Monolayers on Metals. *Acc. Chem. Res.* **2008**, *41* (6), 721–729. <https://doi.org/10.1021/ar700284q>.
- (8) Neaton, J. B.; Hybertsen, M. S.; Louie, S. G. Renormalization of Molecular Electronic Levels at Metal-Molecule Interfaces. *Phys. Rev. Lett.* **2006**, *97* (21), 1–4. <https://doi.org/10.1103/PhysRevLett.97.216405>.

- (9) Thygesen, K. S.; Rubio, A. Renormalization of Molecular Quasiparticle Levels at Metal-Molecule Interfaces: Trends across Binding Regimes. *Phys. Rev. Lett.* **2009**, *102* (4), 046802. <https://doi.org/10.1103/PhysRevLett.102.046802>.
- (10) Yuan, L.; Nerngchamnong, N.; Cao, L.; Hamoudi, H.; Del Barco, E.; Roemer, M.; Sriramula, R. K.; Thompson, D.; Nijhuis, C. A. Controlling the Direction of Rectification in a Molecular Diode. *Nat. Commun.* **2015**, *6*. <https://doi.org/10.1038/ncomms7324>.
- (11) Djurovich, P. I.; Mayo, E. I.; Forrest, S. R.; Thompson, M. E. Measurement of the Lowest Unoccupied Molecular Orbital Energies of Molecular Organic Semiconductors. *Org. Electron.* **2009**, *10* (3), 515–520. <https://doi.org/10.1016/j.orgel.2008.12.011>.
- (12) Cahen, D.; Kahn, A. Electron Energetics at Surfaces and Interfaces: Concepts and Experiments. *Adv. Mater.* **2003**, *15* (4), 271–277. <https://doi.org/10.1002/adma.200390065>.
- (13) Aihara, T.; Abd-Rahman, S. A.; Yoshida, H. Metal Screening Effect on Energy Levels at Metal/Organic Interface: Precise Determination of Screening Energy Using Photoelectron and Inverse-Photoelectron Spectroscopies. *Phys. Rev. B* **2021**, *104* (8), 085305. <https://doi.org/10.1103/PhysRevB.104.085305>.
- (14) Bredas, J.-L. Mind the Gap! *Mater. Horiz.* **2014**, *1* (1), 17–19. <https://doi.org/10.1039/C3MH00098B>.
- (15) Kahn, A. Fermi Level, Work Function and Vacuum Level. *Mater. Horiz.* **2016**, *3* (1), 7–10. <https://doi.org/10.1039/C5MH00160A>.
- (16) Sworakowski, J. How Accurate Are Energies of HOMO and LUMO Levels in Small-Molecule Organic Semiconductors Determined from Cyclic Voltammetry or Optical Spectroscopy? *Synth. Met.* **2018**, *235*, 125–130.

<https://doi.org/10.1016/j.synthmet.2017.11.013>.

- (17) Beebe, J. M.; Kim, B.; Gadzuk, J. W.; Daniel Frisbie, C.; Kushmerick, J. G. Transition from Direct Tunneling to Field Emission in Metal-Molecule-Metal Junctions. *Phys. Rev. Lett.* **2006**, *97* (2), 26801. <https://doi.org/10.1103/PhysRevLett.97.026801>.
- (18) Beebe, J. M.; Kim, B.; Frisbie, C. D.; Kushmerick, J. G. Measuring Relative Barrier Heights in Molecular Electronic Junctions with Transition Voltage Spectroscopy. *ACS Nano* **2008**, *2* (5), 827–832. <https://doi.org/10.1021/nn700424u>.
- (19) Song, X.; Han, B.; Yu, X.; Hu, W. The Analysis of Charge Transport Mechanism in Molecular Junctions Based on Current-Voltage Characteristics. *Chem. Phys.* **2020**, *528* (September 2019), 110514. <https://doi.org/10.1016/j.chemphys.2019.110514>.
- (20) Song, X.; Yu, X.; Hu, W. Model Study on the Ideal Current–Voltage Characteristics and Rectification Performance of a Molecular Rectifier under Single-Level-Based Tunneling and Hopping Transport. *J. Phys. Chem. C* **2020**, *124* (44), 24408–24419. <https://doi.org/10.1021/acs.jpcc.0c06647>.
- (21) Capozzi, B.; Xia, J.; Adak, O.; Dell, E. J.; Liu, Z.-F.; Taylor, J. C.; Neaton, J. B.; Campos, L. M.; Venkataraman, L. Single-Molecule Diodes with High Rectification Ratios through Environmental Control. *Nat. Nanotechnol.* **2015**, *10* (6), 522–527. <https://doi.org/10.1038/nnano.2015.97>.
- (22) Mirjani, F.; Thijssen, J. M.; van der Molen, S. J. Advantages and Limitations of Transition Voltage Spectroscopy: A Theoretical Analysis. *Phys. Rev. B* **2011**, *84* (11), 115402. <https://doi.org/10.1103/PhysRevB.84.115402>.
- (23) Li, H.; Su, T. A.; Zhang, V.; Steigerwald, M. L.; Nuckolls, C.; Venkataraman, L.



- Electric Field Breakdown in Single Molecule Junctions. *J. Am. Chem. Soc.* **2015**, *137* (15), 5028–5033. <https://doi.org/10.1021/ja512523r>.
- (24) Gehring, P.; Thijssen, J. M.; Van Der Zant, H. S. J. Single-Molecule Quantum-Transport Phenomena in Break Junctions. *Nat. Rev. Phys.* **2019**, *1* (6), 381–396. <https://doi.org/10.1038/s42254-019-0055-1>.
- (25) Fereiro, J. A.; McCreery, R. L.; Bergren, A. J. Direct Optical Determination of Interfacial Transport Barriers in Molecular Tunnel Junctions. *J. Am. Chem. Soc.* **2013**, *135* (26), 9584–9587. <https://doi.org/10.1021/ja403123a>.
- (26) Liu, H.; Chen, L.; Zhang, H.; Yang, Z.; Ye, J.; Zhou, P.; Fang, C.; Xu, W.; Shi, J.; Liu, J.; Yang, Y.; Hong, W. Single-Molecule Photoelectron Tunnelling Spectroscopy. *Nat. Mater.* **2023**, *22* (8), 1007–1012. <https://doi.org/10.1038/s41563-023-01591-4>.
- (27) Gobbi, M.; Pietrobon, L.; Atxabal, A.; Bedoya-Pinto, A.; Sun, X.; Golmar, F.; Llopis, R.; Casanova, F.; Hueso, L. E. Determination of Energy Level Alignment at Metal/Molecule Interfaces by in-Device Electrical Spectroscopy. *Nat. Commun.* **2014**, *5* (1), 4161. <https://doi.org/10.1038/ncomms5161>.
- (28) Atxabal, A.; Braun, S.; Arnold, T.; Sun, X.; Parui, S.; Liu, X.; Gozálvez, C.; Llopis, R.; Mateo-Alonso, A.; Casanova, F.; Ortmann, F.; Fahlman, M.; Hueso, L. E. Energy Level Alignment at Metal/Solution-Processed Organic Semiconductor Interfaces. *Adv. Mater.* **2017**, *29* (19), 1606901. <https://doi.org/10.1002/adma.201606901>.
- (29) Arnold, T.; Atxabal, A.; Parui, S.; Hueso, L. E.; Ortmann, F. Hot Electrons and Hot Spins at Metal–Organic Interfaces. *Adv. Funct. Mater.* **2018**, *28* (15), 1706105. <https://doi.org/10.1002/adfm.201706105>.
- (30) Atxabal, A.; Arnold, T.; Parui, S.; Zuccatti, E.; Cinchetti, M.; Casanova, F.;

- Ortmann, F.; Hueso, L. E. Molecular Spectroscopy in a Solid-State Device. *Mater. Horiz.* **2019**, 6 (8), 1663–1668. <https://doi.org/10.1039/C9MH00218A>.
- (31) Bell, L. D.; Kaiser, W. J. Observation of Interface Band Structure by Ballistic-Electron-Emission Microscopy. *Phys. Rev. Lett.* **1988**, 61 (20), 2368–2371. <https://doi.org/10.1103/PhysRevLett.61.2368>.
- (32) Prietsch, M. Ballistic-Electron Emission Microscopy (BEEM): Studies of Metal/Semiconductor Interfaces with Nanometer Resolution. *Phys. Rep.* **1995**, 253 (4), 163–233. [https://doi.org/10.1016/0370-1573\(94\)00082-E](https://doi.org/10.1016/0370-1573(94)00082-E).
- (33) Jiang, J. S.; Pearson, J. E.; Bader, S. D. Direct Determination of Energy Level Alignment and Charge Transport at  $\text{Metal}/\text{Alq}_3$  Interfaces via Ballistic-Electron-Emission Spectroscopy. *Phys. Rev. Lett.* **2011**, 106 (15), 156807. <https://doi.org/10.1103/PhysRevLett.106.156807>.
- (34) Atxabal, A.; Arnold, T.; Parui, S.; Hutsch, S.; Zuccatti, E.; Llopis, R.; Cinchetti, M.; Casanova, F.; Ortmann, F.; Hueso, L. E. Tuning the Charge Flow between Marcus Regimes in an Organic Thin-Film Device. *Nat. Commun.* **2019**, 10 (1), 2089. <https://doi.org/10.1038/s41467-019-10114-2>.
- (35) Meir, Y.; Wingreen, N. S. Landauer Formula for the Current through an Interacting Electron Region. *Phys. Rev. Lett.* **1992**, 68 (16), 2512–2515. <https://doi.org/10.1103/PhysRevLett.68.2512>.
- (36) Simmons, J. G. Generalized Formula for the Electric Tunnel Effect between Similar Electrodes Separated by a Thin Insulating Film. *J. Appl. Phys.* **1963**, 34 (6), 1793–1803. <https://doi.org/10.1063/1.1702682>.
- (37) Filatova, E. O.; Konashuk, A. S. Interpretation of the Changing the Band Gap of Al<sub>2</sub>O<sub>3</sub> Depending on Its Crystalline Form: Connection with Different Local

- Symmetries. *J. Phys. Chem. C* **2015**, *119* (35), 20755–20761.  
<https://doi.org/10.1021/acs.jpcc.5b06843>.
- (38) Jia, C.; Guo, X. Molecule–Electrode Interfaces in Molecular Electronic Devices. *Chem. Soc. Rev.* **2013**, *42* (13), 5642–5660.  
<https://doi.org/10.1039/C3CS35527F>.
- (39) Sowa, J. K.; Mol, J. A.; Briggs, G. A. D.; Gauger, E. M. Beyond Marcus Theory and the Landauer–Büttiker Approach in Molecular Junctions: A Unified Framework. *J. Chem. Phys.* **2018**, *149* (15).  
<https://doi.org/10.1063/1.5049537>.
- (40) Datta, S. *Quantum Transport: Atom to Transistor*; Cambridge University Press: Cambridge, UK ; New York, 2005.
- (41) Nitzan, A. *Chemical Dynamics in Condensed Phases: Relaxation, Transfer and Reactions in Condensed Molecular Systems*; Oxford university press, 2006.
- (42) Migliore, A.; Nitzan, A. Nonlinear Charge Transport in Redox Molecular Junctions: A Marcus Perspective. *ACS Nano* **2011**, *5* (8), 6669–6685.  
<https://doi.org/10.1021/nn202206e>.
- (43) Fann, W. S.; Storz, R.; Tom, H. W. K.; Bokor, J. Electron Thermalization in Gold. *Phys. Rev. B* **1992**, *46* (20), 13592–13595.  
<https://doi.org/10.1103/PhysRevB.46.13592>.
- (44) Seah, M. P.; Dench, W. A. Quantitative Electron Spectroscopy of Surfaces: A Standard Data Base for Electron Inelastic Mean Free Paths in Solids. *Surf. Interface Anal.* **1979**, *1* (1), 2–11. <https://doi.org/10.1002/sia.740010103>.
- (45) Bevan, K. H.; Hossain, Md. S.; Iqbal, A.; Wang, Z. Exploring Bridges between Quantum Transport and Electrochemistry. I. *J. Phys. Chem. C* **2016**, *120* (1), 179–187. <https://doi.org/10.1021/acs.jpcc.5b09653>.

- (46) Hossain, Md. S.; Bevan, K. H. Exploring Bridges between Quantum Transport and Electrochemistry. II. A Theoretical Study of Redox-Active Monolayers. *J. Phys. Chem. C* **2016**, *120* (1), 188–194. <https://doi.org/10.1021/acs.jpcc.5b09654>.
- (47) Cohen, A. J.; Mori-Sánchez, P.; Yang, W. Insights into Current Limitations of Density Functional Theory. *Science* **2008**, *321* (5890), 792–794. <https://doi.org/10.1126/science.1158722>.
- (48) Migliore, A.; Schiff, P.; Nitzan, A. On the Relationship between Molecular State and Single Electron Pictures in Simple Electrochemical Junctions. *Phys. Chem. Chem. Phys.* **2012**, *14* (40), 13746. <https://doi.org/10.1039/c2cp41442b>.